Geochemistry Geophysics Geosystems G3

Article
Volume 14, Number 10
3 October 2013
doi: 10.1002/ggge.20268
ISSN: 1525-2027

Published by AGU and the Geochemical Society

Interrelation between rifting, faulting, sedimentation, and mantle serpentinization during continental margin formation—including examples from the Norwegian Sea

Lars H. Rüpke
GEOMAR Helmholtz Centre for Ocean Research Kiel, Dynamics of the Ocean Floor, Wischhofstr. 1-3 DE-24148 Kiel, Germany (lruepke@geomar.de)

Daniel W. Schmid
Physics of Geological Processes, University of Oslo, Oslo, Norway

GeoModelling Solutions GmbH, Zurich, Switzerland

Marta Perez-Gussinye
Department of Earth Sciences, Royal Holloway, University of London, London, UK

Ebbe Hartz
Det norske oljeselskap, Oslo, Norway

The Centre for Earth Evolution and Dynamics, University of Oslo, Oslo, Norway

[1] The conditions permitting mantle serpentinization during continental rifting are explored within 2-D thermotectonostratigraphic basin models, which track the rheological evolution of the continental crust, account for sediment blanketing effects, and allow for kinetically controlled mantle serpentinization processes. The basic idea is that the entire extending continental crust has to be brittle for crustal scale faulting and mantle serpentinization to occur. The isostatic and latent heat effects of the reaction are fully coupled to the structural and thermal solutions. A systematic parameter study shows that a critical stretching factor exists for which complete crustal embrittlement and serpentinization occurs. Increased sedimentation rates shift this critical stretching factor to higher values as sediment blanketing effects result in higher crustal temperatures. Sediment supply has therefore, through the temperature-dependence of the viscous flow laws, strong control on crustal strength and mantle serpentinization reactions are only likely when sedimentation rates are low and stretching factors high. In a case study for the Norwegian margin, we test whether the inner lower crustal bodies (LCB) imaged beneath the Møre and Vøring margin could be serpentinized mantle. Multiple 2-D transects have been reconstructed through the 3-D data set by Scheck-Wenderoth and Maystrenko (2011). We find that serpentinization reactions are possible and likely during the Jurassic rift phase. Predicted thicknesses and locations of partially serpentinized mantle rocks fit to information on LCBs from seismic and gravity data. We conclude that some of the inner LCBs beneath the Norwegian margin may be partially serpentinized mantle.

Components: 12,385 words, 12 figures, 3 tables.

Keywords: serpentine; rifted margins; Norway; basin modeling.

Index Terms: 8105 Continental margins: divergent: Tectonophysics; 8109 Continental tectonics: extensional: Tectonophysics; 8110 Continental tectonics: general: Tectonophysics; 8169 Sedimentary basin processes: Tectonophysics; 1212

Earth's interior: composition and state: Geodesy and Gravity; 8124 Earth's interior: composition and state: Geodesy and Gravity; 0905 Continental structures: Exploration Geophysics; 0545 Modeling: Computational Geophysics; 1952 Modeling: Informatics; 4255 Numerical modeling: Oceanography: General; 4316 Physical modeling: Natural Hazards.

Received 9 July 2013; **Revised** 6 September 2013; **Accepted** 6 September 2013; **Published** 3 October 2013.

Rüpke, L. H., D. W. Schmid, M. Perez-Gussinye, and H. Hartz (2013), Interrelation between rifting, faulting, sedimentation, and mantle serpentinization during continental margin formation—Including examples from the Norwegian Sea, *Geochem. Geophys. Geosyst.*, *14*, 4351–4369, doi:10.1002/ggge.20268.

1. Introduction

[2] The rupture of continents and the creation of new oceanic basins create passive continental margins that are traditionally categorized into volcanic and nonvolcanic margins according to their degree of magmatism [*Sawyer et al*., 2007]. Nonvolcanic margins are either associated with structures typical for the Iberian-Newfoundland conjugates such as hyperextension of the continental crust, detachment faulting, exhumation of partially serpentinized mantle, wide continent-ocean transition zones, and thin sediment sequences [e.g., *Ranero and Perez-Gussinye*, 2010; *Reston and McDermott*, 2011; *Whitmarsh et al*., 2001], or with structures often observed in the South Atlantic such as wide regions with thinned continental crust, largely removed mantle lithosphere, and thicker sediment sequences [e.g., *Huismans and Beaumont*, 2011]. Both types of nonvolcanic margin show only limited magmatic activity prior to seafloor spreading [e.g., *Boillot and Froitzhelm*, 2001]. In contrast, volcanic passive margins, such as the Norwegian margin, often feature extensive intrusive and extrusive magmatic activity at the time of breakup, which accommodates parts of the extension [e.g., *Geoffroy*, 2005]. Thick sedimentary sequences and seaward-dipping seismic reflectors are typical for margins of this type, which often also show an over-thickened basaltic crust and lower crustal bodies (LCB) that may represent underplates of mantle melts [e.g., *Gernigon et al*., 2006; *White et al*., 1987]. Volcanic and nonvolcanic margins thus differ in their geological structures and processes that shape them. Despite these differences, some concepts and ideas developed for nonvolcanic margin formation may also be valid for their volcanic counterparts. For example, the classic interpretation that LCBs imaged beneath volcanic margins originate from magmatic underplates is increasingly challenged. *Gernigon et al*. [2004] summarized different possible origins for the LCB imaged beneath the Gjallar Ridge in the outer Vøring basin offshore Norway—ranging from magmatic underplates, over higher grade metamorphic rocks, to partially serpentinized mantle. More recently, *Lundin and Dore* [2011] have argued that the inner LCBs along the Norwegian continental margin may be of serpentinized mantle origin, while the outer ones are more likely formed by mantle melting. This suggests that margins classified as volcanic may have undergone a nonvolcanic phase throughout their evolution. If so, the questions arises what this implies for the structural and thermal evolution of volcanic margins.

[3] Most ideas for mantle serpentinization during margin formation have been developed for the Iberian-Newfoundland nonvolcanic conjugates [*Perez-Gussinye and Reston*, 2001; *Perez-Gussinye et al*., 2006; *Reston and McDermott*, 2011], where low extension rates and/or a low mantle potential temperature provide favorable conditions for mantle serpentinization to occur. In contrast, volcanic margins, like the Norwegian margin, experience strong magmatic activity during their formation pointing to elevated mantle temperatures. In addition, thick sedimentary sequences, of up to 15 km and more in the case of the Norwegian margin, effectively heat the (lower) crust. This may inhibit crustal-scale faulting and results in sub-Moho temperatures that are possibly outside the thermal stability field of serpentine minerals. Mantle serpentinization thus appears less likely during the formation of volcanic margin. In this study, we use an integrated 2-D basin modeling approach to systematically explore the interrelation between continental extension, sedimentation, and the rheological evolution of the lower crust. The goal is to evaluate under which conditions mantle serpentinization may occur. These theoretical insights then form the basis of a case study for the Møre and Vøring margin offshore Norway, in which we use numerical modeling to evaluate whether the Norwegian margin may have experienced a nonvolcanic margin phase throughout the Jurassic and whether the observed inner LCBs may, in fact, represent partially serpentinized mantle rather than magmatic underplates.

2. Modeling Framework

2.1. Background on Serpentinization

[4] Serpentinization, the transformation of a dry peridodite to a wet serpentinite, has received considerable attention in the passive margin community [e.g., *Skelton et al*., 2005] with Iberian-type nonvolcanic margins clearly showing wide continent-ocean-transition zones, where serpentinized mantle is exhumed. The interest in serpentinization reactions roots in the drastic petrophysical changes a rock undergoes during the reaction. For example, the complete transformation of a dry peridotite to a wet serpentinite involves a volume increase of ~40% and a significant decrease in seismic wave speed. This implies that partially serpentinized mantle can have seismic and gravity signals similar to crustal rocks (or magmatic underplates). As mantle serpentinization reactions result in a density reduction and the release of latent heat, they may result in anomalous subsidence and heat flow patterns. Finally, the lowered strength of partially serpentinized rocks can have profound implications for strain partitioning within continental rift zones.

[5] In its most simplified form, the serpentinization reaction can be written as the conversion of forsterite into serpentine plus brucite through the addition of water:

$$\begin{array}{l} 2Mg_2SiO_4 + 3H_2O = Mg_3Si_2O_5(OH)_4 + Mg(OH)_2 \\ \text{olivine} \quad + \text{water} = \text{serpentine} \quad + \text{brucite} \end{array} \quad (1)$$

[6] In nature, the reaction is more complex and involves differing reaction pathways as well as reaction components. Furthermore, magnetite may form and even methane by Fischer-Tropsch type reactions. More details are given in the review by *Skelton et al*. [2005]. The conditions under which mantle serpentinization occurs during passive margin formation have been explored by *Perez-Gussinye et al*. [2006] and *Perez-Gussinye and Reston* [2001]. The basic idea is that seawater needs to get in contact with cold (<550°C) lithospheric mantle rocks. For this to occur, crustal-scale brittle faulting is necessary. However, in normal continental crust, parts of the lower (and sometimes upper) crust are ductile and pose a permeability barrier for seawater, thereby impeding mantle serpentinization. Crustal-scale embrittlement can occur during extension when the crust is progressively cooled. At this stage, crustal scale faulting becomes possible and can provide the pathways for seawater to reach and react with cold mantle rocks to make serpentine (Figure 1a).

[7] One key prediction of the *Perez-Gussinye and Reston* [2001] model is that a critical stretching factor is needed for mantle serpentinization to occur. The exact value depends on many parameters including rheology, extension rate, and temperature. For example, rapid extension results in high temperatures and strain rates within the rift zone, which both favor ductile deformation and relatively more extension is necessary for complete crustal embrittlement. During slow extension, strain rates, and temperatures within the rift zone are lower, which in turn favors brittle deformation. *Perez-Gussinye and Reston* [2001] explored a wide parameter range and found that critical stretching factors are consistently above 3 suggesting that serpentinization is only likely in high extension settings like passive rifted margins.

2.2. Basin Modeling Framework

[8] We use the basin model TecMod as a platform and have extended it to also account for mantle serpentinization reactions. TecMod's basin reconstruction approach is based in the coupling of a thermotectonostratigraphic forward model to an inverse scheme for automated model parameter update. The technical details can be found in *Rüpke et al*. [2008, 2010]. The two-dimensional forward model is locally based on pure-shear kinematics and resolves simultaneously for differential thinning, flexural isostasy, heat transfer, sedimentation, and compaction on a Lagrangian finite-element mesh. The inverse module refines the crustal and mantle stretching factors as well as sedimentation rates in time and space for automated stratigraphy fitting. Taking the observed seismic stratigraphy as input, sedimentary basins are iteratively reconstructed by refining the model parameters (stretching factors and sedimentation rates) until the forward model results in a basin architecture that matches the input stratigraphy.

[9] The general forward modeling strategy is that the structural and thermal solutions are in equilibrium after every simulation time step. This is achieved by resolving fully coupled for deep lithosphere and shallow sedimentary basin processes. During every time step, the entire computational mesh is deformed with the pure-shear mantle and crustal stretching factors, new sediment packages are deposited and become part of the computational domain, and flexural isostasy is ensured by further movement of the mesh in the vertical

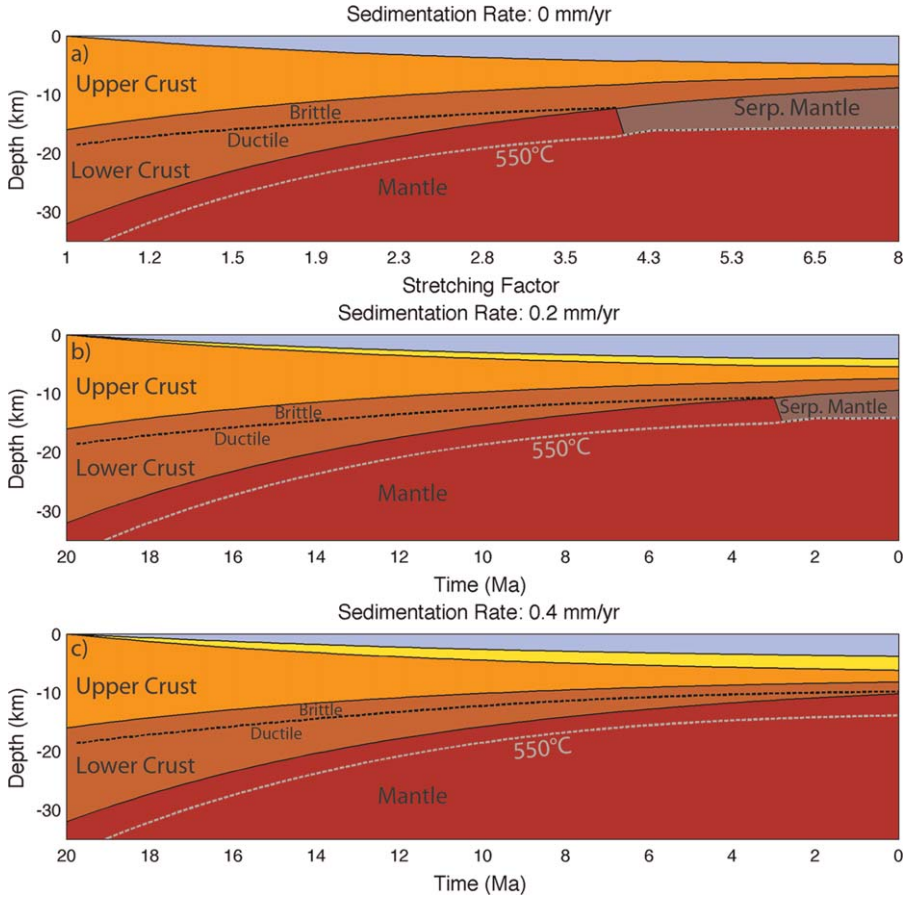

Figure 1. Rheological and thermal evolution of extending lithosphere for different sedimentation rates. (a) The case without sedimentation. Progressive stretching leads to complete crustal embrittlement and mantle serpentinization upon a critical stretching factor. (b) The same setup but with a sedimentation rate of 0.2 mm/yr. Now a higher stretching factor is required for the crust to become entirely brittle and the mantle is slightly hotter as a consequence of sediment blanketing effects. (c) A sedimentation rate of 0.4 mm/yr is enough to prevent crustal embrittlement throughout the entire numerical experiment and mantle temperatures are even higher. This shows the strong effect of sedimentation on the rheological and thermal evolutions of extending lithosphere.

direction. In this study, we have modified TecMod's forward model so that it also resolves the onset, extent, and consequences of mantle serpentinization.

2.3. Stress-Strain Relationships

[10] Constraining the conditions under which the entire crust becomes brittle requires tracking the rheological evolution of the lithosphere. The brittle yield stress is calculated according to *Ranalli and Murphy* [1987]:

$$\sigma_{brittle} = \gamma P_{litho}(1 - \iota) \tag{2}$$

[11] γ is a parameter that depends on the type of faulting (0.75 for normal faulting), ι describes the pore pressure ratio, which, in the hydrostatic case, is the ratio between fluid and solid densities, and P_{litho} is the lithostatic pressure. The viscous deviatoric stress is calculated from a dislocation creep flow law:

$$\sigma_{vis} = \left(\frac{\dot{\varepsilon}}{A}\right)^{\frac{1}{n}} \exp\left(\frac{E}{nRT}\right) \tag{3}$$

where $\dot{\varepsilon}$ is strain rate, n the power law coefficient, A the prefactor, R the universal gas constant, E activation energy, and T temperature in Kelvin. Table 1 summarizes the explored viscous flow laws.

[12] The final unknown is the strain rate in equation (3), which can be calculated from the pure-

Table 1. Rheological Parameters

Lithology	n	A (Pa^{-n} s^{-1})	E (kJ mol^{-1})	References
Wet quartzite	2.4	1.3×10^{-20}	134	*Kronenberg and Tullis* [1984]
Dry quartzite	2.9	5×10^{-25}	149	*Koch* [1983]
Anorthosite	3.2	5.6×10^{-23}	238	*Shelton and Tullis* [1981]
Aggregate	3	4.9×10^{-24}	192.4	*Tullis et al.* [1991]
Dry olivine	3	1×10^{-13}	500	*Newman and White* [1997]

shear stretching factors computed by the basin model:

$$\dot{\varepsilon} = \frac{\log(\delta)}{\Delta t} \tag{4}$$

where δ is the incremental crustal stretching factor. Note that all presented models assume uniform extension of the crust and mantle; if differential thinning were assumed different strain rates for the crust and mantle would have to be computed. Serpentinization can occur when the entire crust becomes brittle, i.e., within the entire crust the brittle yield stress is lower than the ductile stress. This implementation appears to us realistic but a few implications/limitations should be mentioned. First, serpentinization can only occur during the synrift phase. At postrift times, all strain rates computed from equation (4) are zero and thereby also all deviatoric stresses. On the one hand, this is a valid assumption as faulting is associated with active deformation/extension. However, limited deformation may also occur in the postrift, on the other hand, and some faults may be created or remain open for water circulation; this is not accounted for in the current implementation. Second, the implied circulation of seawater through the crust and sediments is likely to have a hydrothermal cooling effect. For example, according to equation (1) the complete serpentinization of 3300 kg forsterite in a cubic meter of mantle rock requires ~634 kg of water. While these are significant amounts of water, limited degrees of serpentinization (<20%) in combination with a single pass scenario, i.e., one in which all down-flowing water is completely consumed by the reaction and no hydrothermal convection cell forms, is not likely to have a major effect on the crustal thermal structure and hydrothermal cooling is not accounted for in this study. Third, our implementation is based on pure-shear kinematics. Dynamic models are better suited for understanding the feedbacks between strain partitioning within extending lithosphere and mantle serpentinization reactions but are not yet fit for detailed basin reconstruction studies. We therefore chose to stay within the semikinematic framework.

2.4. Serpentinization Rates

[13] Tracking the rheological evolution of the lithosphere allows us to explore the conditions when mantle serpentinization can occur. The next step is to determine the rate and extent of serpentinization. The determination of a single rate law describing the progress of serpentinization is complex as the reaction progress is controlled by the initial starting material, grain size distribution, temperature, water supply, intergranular diffusion and serpentine dissolution rate [*Malvoisin et al.*, 2012b; *Martin and Fyfe*, 1970; *Wegner and Ernst*, 1983]. Nevertheless, experimental data indicate that a parameterization in terms of temperature is a valid simplification. Here we follow the approaches of *Iyer et al.* [2010] and *Emmanuel and Berkowitz* [2006] and express the rate of serpentinization in terms of a temperature-dependent forsterite conversion rate:

$$\frac{\partial \rho_{fo}}{\partial t} = -k(T)\rho_{fo} \tag{5}$$

where ρ_{fo} is the remaining mass of forsterite (unreacted mantle rock) and $k(T)$ is the experimentally determined rate of serpentinization, which depends on temperature (Figure 2). The kinetic rate is approximated by a simple bell-shaped function [*Emmanuel and Berkowitz*, 2006]. In the laboratory, serpentinization of ground olivine occurs within years [*Martin and Fyfe*, 1970] leading *Wegner and Ernst* [1983] to conclude that serpentinization is probably fast (instantaneous) on geological timescales. However, observations from natural systems including passive margins and the "Rainbow" and "Lost City" hydrothermal fields suggest that reactions rates are much slower in nature (10^4–10^6 years) [*Fruh-Green et al.*, 2003; *Skelton et al.*, 2005]. In this study, we use reaction rates that lead to complete serpentinization on a 10^6 years timescale, which is still fast with respect to typical durations of rifting events. The degree of serpentinization during the formation of passive margins is therefore not likely to be limited by reaction kinetics but rather by water supply or even mechanical effects inhibiting dilatational deformation. In order to avoid unrealistically high degrees of serpentinization, we set an upper limit of 20% for the degree of serpentinization, which is based on the inferred degree of serpentinization

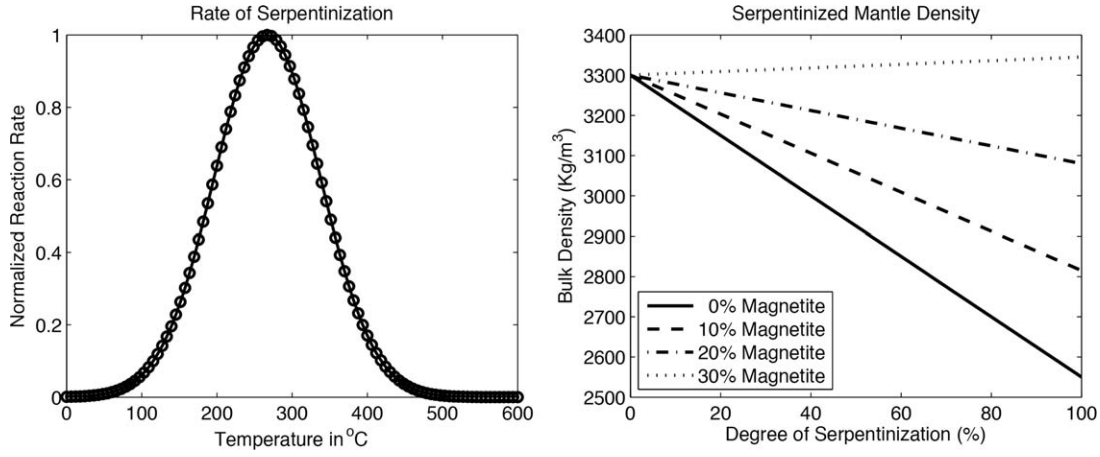

Figure 2. Normalized rate of mantle serpentinization (left graph) and bulk density of partially serpentinized rocks (right graph).

from seismic and gravity studies along passive margins.

[14] Deserpentinization takes place if serpentinized rocks move out of their thermal stability limit. This can, for example, happen during the postrift following a very slow synrift phase, when heating of the crust through the deposition of sediments dominates over postrift cooling. As deserpentinization rate, we use the maximum of the rate determined by equation (5).

[15] The reaction of a dry peridotite to a wet serpentinite results in a reduction in bulk density. We follow *Skelton et al*. [2005] and express the change in bulk density as a function of the relative proportions of serpentine (2550 kg/m^3) and magnetite (5200 kg/m^3) minerals forming during the reaction:

$$\rho_{serp} \approx \xi\{(X_{Mt}5200) + [(1 - X_{Mt})2550]\} + (1 - \xi)3300 \quad (6)$$

[16] X_{Mt} is the relative proportion of magnetite and ζ is the reaction progress. If $X_{Mt} < 0.3$, total serpentinization will cause a reduction in density. Figure 2 illustrates how the bulk density changes during serpentinization. General statements on the likely amount of magnetite forming during the reaction remain difficult to make [*Malvoisin et al*., 2012a; *Oufi et al*., 2002]. Large fractions of magnetite are, however, unlikely to form at low degrees of serpentinization and we therefore use a constant value of 10% magnetite forming during the reaction. The density changes associated with the partial serpentinization of mantle rocks are accounted for in the isostatic balance of the forward basin model and may result in relative uplift (or subsidence in the case of deserpentinization).

2.5. Thermal Effects

[17] The forward basin model accounts for advective and diffusive heat transfer as well as radiogenic heating. For this study, we have modified the energy balance equation to also account for latent heat effects. The latent heat of the reaction is $H = 2.9 \times 10^5$ J/kg [*Emmanuel and Berkowitz*, 2006], which is roughly equal to a temperature rise of 300°C for the complete transformation. The energy conservation equation (in terms of temperature) can be written as:

$$(\rho c_p)_{bulk} \frac{\partial T}{\partial t} = \nabla \cdot (\lambda_{eff} \nabla T) - (\rho c_p)_{bulk} \vec{v} \cdot \nabla T + Q_{radio} - H \frac{\partial \rho_{fo}}{\partial t} \quad (7)$$

where λ_{eff} is the effective thermal conductivity, which is the geometric mean of rock/grain and pore fluid conductivity. A change in temperature (left-hand side) is related to heat diffusion (1. term on the rhs), heat advection (2. term on the rhs), radiogenic heating (3. term on the rhs), and the rate of serpentinization (last term on the rhs). It is clear that equations (5) and (7) are coupled (both depend on temperature). The nonlinear system of equation is solved using direct iterations (Picard iterations). In addition, an adaptive time stepping algorithm is used when serpentinization occurs. This is necessary as typical simulation time steps are too large to accurately resolve serpentinization reactions.

3. Sedimentation, Crustal Embrittlement, and Mantle Serpentinization

[18] The described modeling framework allows us to test the idea of stretching induced

Table 2. Summary of Model Parameters

Model Parameter	Value
Lithosphere thickness	125 km
Upper crust	16 km
Lower crust	16 km
Top and bottom temperature	10 and 1300°C
Thermal conductivity (crust and mantle)	2.6 and 3.4 W/m/K
Density (crust and mantle)	2800 and 3300 kg/m^3
Specific heat (crust and mantle)	800 J/kg/K
Thermal expansion coefficient (crust and mantle)	4.4×10^{-5} and 2×10^{-5} K^{-1}
Radiogenic heat (crust)	4.39×10^{-6} W/m^3
e-Fold length radiogenic heating (crust)	10 km
Initial Moho temperature and heat flow	500°C and 72 mW/m^2
Sediment grain density	2700 kg/m^3
Sediment surface porosity	56%
Sediment compaction length scale	0.39 km^{-1}
Sediment grain conductivity	2.5 W/m/K
T-dependence of sediment conductivity	*Deming and Chapman* [1989]
Sediment specific heat	1000 J/kg/K
Sediment radiogenic heat	1×10^{-6} W/m^3
Serpentinization rate	10^{-13} s^{-1}
Fraction of magnetite	10%
Thermal stability limit of serpentine at relevant pressure conditions	550°C, *Ulmer and Trommsdorff* [1995]

serpentinization within realistic basin reconstruction case studies. We will first present results from systematic numerical experiments that explore the interrelation between stretching, faulting, sedimentation, and mantle serpentinization before applying the model to the Norwegian passive margin.

3.1. Reference Case

[19] All forward models presented in this section share the common setup summarized in Table 2. The thermal parameters result in an initial Moho temperature of 500°C. A 20 Ma synrift phase with a sinusoidal distribution of stretching factors of up to 5 is followed by a 50 Ma long postrift phase. This setup leads to strain rates of 2.6×10^{-15} s^{-1} in the rift center during the synrift phase. We assume a wet quartzite rheology for the upper crust, an aggregate rheology for the lower crust, and a dry olivine rheology for the mantle (Table 1). Sedimentation is not included in this initial setup.

[20] A first simple forward run based on this setup illustrates the concept of stretching induced serpentinization. Figure 3 shows (a) the stress distribution at the end of the synrift phase along with (b) the cumulative stretching factors. At the distal parts of the rift, where stretching factors are low, the upper and lower crust both show thick zones of ductile deformation marked by a low differential stress (Figure 3c). Further toward the rift center, at a stretching factor of 2.3, the upper crust becomes brittle but the lower crust still deforms viscously (Figure 3d). Beyond a critical stretching factor of 3.6 the entire crust is brittle (Figure 3e) and serpentinization can occur with a rate and extent that is controlled by the temperature field. Figure 4a visualizes the temperature field which shows that the sub-Moho mantle progressively cooled during extension so that about 7.5 km of lithospheric mantle is within the thermal stability field of serpentine at the end of the synrift phase (compared to ~5.5 km prior to rifting). The density plot illustrates the reduction in bulk density resulting from partial serpentinization following complete crustal embrittlement (Figure 4b). This reduction in bulk density impacts basement subsidence.

[21] Figure 5a illustrates the effect by showing synrift and postrift total subsidence curves for different degrees of mantle serpentinization for the same model setup as in Figure 3. Striking is the reduced synrift subsidence (or relative uplift with respect to a model without serpentinization). It is clear that serpentinization reactions have a first order and permanent, isostatic uplift effect. For the particular setup discussed here, every additional 20% of mantle serpentinization results in about 275 m of uplift so that the simulation with 80% serpentinization results in about 1100 m of relative uplift with respect to the reference model. An alternative back-of-envelope way of computing serpentinization induced uplift is a simple isostatic balance:

$$h = s\frac{(\rho_m - \rho_s)}{(\rho_m - \rho_i)} \tag{8}$$

where ρ is density (kg/m^3) and the subscripts (m, s, i) refer to mantle, serpentinized mantle, and infill; h is uplift in meters and s the thickness of the partially serpentinized layer in meters. Taking the above example (7.5 km of 20% serpentinized mantle with a density 3203 kg/m^3, a mantle density of 3300 kg/m^3, and water (1000 kg/m^3) as infill) we arrive at a comparable uplift of 315 m. By combining equations (6) and (8) it is this therefore straightforward to make a quick estimate on reaction-induced uplift but it should be kept in mind that, for example, thermal and flexural effects are, of course, not accounted for in equation (8).

[22] The thermal effects of mantle serpentinization are illustrated in Figure 5b, where the heat flow

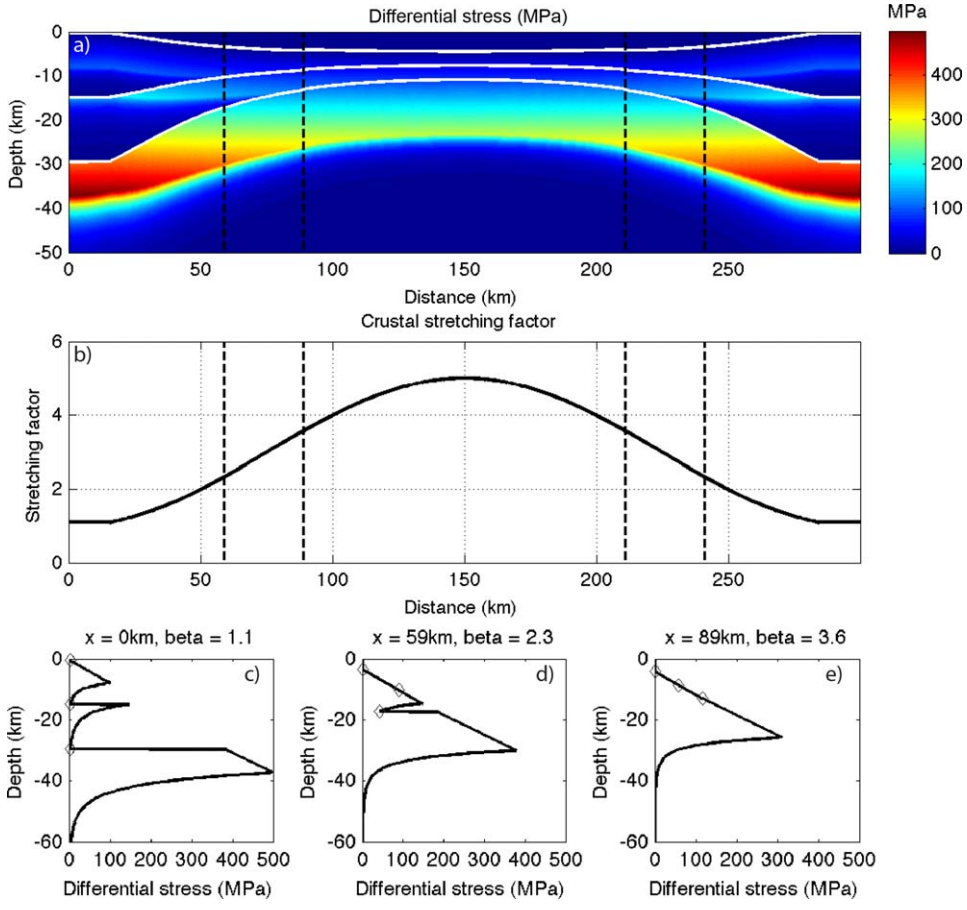

Figure 3. (top) The differential stress distribution at the end of the synrift phase. White lines mark the top crust, the boundary between upper and lower crust, and the Moho. Vertical dashed lines indicate when the upper and lower crusts become brittle, respectively. Note the dark blue zones that indicate viscous creep in the upper and lower crust at the margins of the rift zone. (middle) The distribution of crustal stretching factors. Figures 3c–3e show differential stress profiles for the dashed lines in Figure 3b (diff. stress at $x = 0$, diff. stress when the upper crust becomes brittle, diff. stress when the entire crust becomes brittle). Grey diamonds mark the location of the top basement, boundary of the upper and lower crust, and the Moho. Strain rates increase toward the rift center from 1.5e−16 s^{-1} (Figure 3c), over 1.4e−15 s^{-1} (Figure 3d), to 2.6e−15 s^{-1} (Figure 3e).

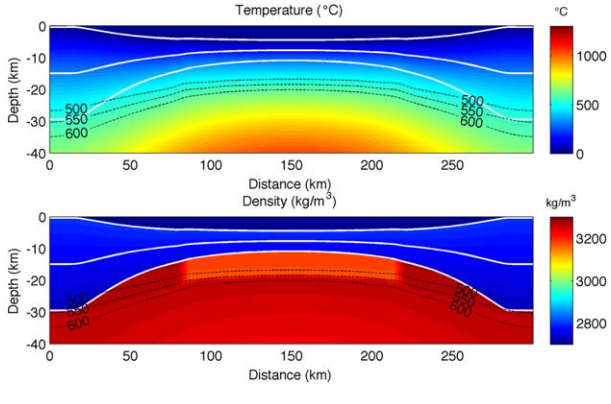

Figure 4. (top) The temperature field at the end of the synrift phase. Dashed black contours show temperature isolines. While lines mark the crustal geometry. (bottom) The density field. Note the low density serpentinized mantle body in the center of the rift zone.

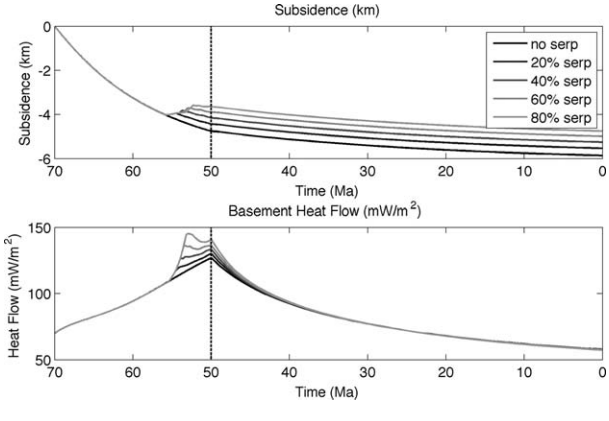

Figure 5. Evolution of basement subsidence and basement heat flow in the rift center (cf. Figure 3) as a function of serpentinization. Partial mantle serpentinization results in permanent basement uplift and a transient increase in basement heat flow.

curves corresponding to the subsidence curves in Figure 5a are plotted. A transient increase in basement heat flow occurs as a consequence of the latent heat release during the reaction. This increase in basement heat flow is significant and can reach values of >30 mW/m^2 with respect to a model without serpentinization. Again, an alternative simplified way of looking at this is to consider the latent heat effect directly: 2.9×10^5 J/kg are release by the reaction. Multiplying this number by 3300 kg/m^3 forsterite available as well as a serpentinized mantle thickness of 7500 m and taking an effective reaction time of 3.5 my (Figure 5) we arrive at an average additional heat flux of 65 mW/m^2 for the complete reaction and 52 mW/m^2 for 80% serpentinization. This simplified argument assumes that all heat is rapidly lost vertically and results in higher yet similar numbers as the full numerical solution. This shows that the latent heat effect is significant and that its relative importance scales with stretching factor, extension rate, and degree of serpentinization. The lower the Moho temperature and thereby the "background" heat flow at the time of crustal embrittlement the more important becomes the reaction-induced relative increase in basement heat flow.

[23] In summary, mantle serpentinization occurs upon complete crustal embrittlement and results in permanent synrift uplift and a transient increase in basement heat flow. Both effects are significant and affect a basin's thermal and structural evolutions. The exact conditions under which serpentinization can occur (i.e., the critical stretching factor) depend on the exact choice of model parameters (e.g., the amount and duration of rifting, initial and transient thermal structure, initial crustal geometry, viscous flow laws, and sedimentation rate). The effects of rift duration, amount of rifting, and sedimentation are discussed in the next section. The thermal parameters can, as we will show later, be constrained in real world case studies through well calibration. A discussion on the effects of using different viscous flow laws on serpentinization can be found in *Perez-Gussinye and Reston* [2001].

3.2. Effects of Sedimentation

[24] Sediments are a first-order feature of sedimentary basins yet the feedbacks between shallow sedimentary and deep mantle processes are often underappreciated. For example, sediments typically have a lower effective thermal conductivity than crustal rocks causing blanketing effects and sediment loading results in additional subsidence. Both, deeper burial and blanketing effects, lead to higher temperatures within the lower crust thereby hampering complete crustal embrittlement. We will illustrate this effect in a series of model runs in which the rift duration, stretching factor, and rate of sediment supply are systematically varied. In these simulations, a laterally constant stretching factor is assumed, rendering the 2-D models quasi 1-D. In addition, a single aggregate flow law (cf. Table 2) is used for both the upper and lower crust; a wet quartzite flow law is assumed for the sediments and an olivine flow law for the mantle. All simulations are run for the synrift phase only.

[25] Figure 6 (top) shows the results of models without sediments as reference. Figure 6a shows how Moho temperatures are affected by the rifting parameters: the longer the rift duration and the higher the stretching factor, the lower is the Moho temperature at the end of the synrift phase. The black contour lines illustrate the associated strain rates for the given rifting parameters. In Figure 6b, the associated effective viscosity $\left(\mu = \frac{\sigma}{2\dot{\varepsilon}}\right)$ of the lower crust at Moho level is plotted. Finally, in Figure 6c the thickness of serpentinized mantle is shown. Beyond the critical stretching factor, up to 8 km of mantle can be serpentinized beneath the Moho. The switch from ductile to brittle deformation in the lower crust at a critical stretching factor is visible in all three subplots. For example, Moho temperatures are slightly elevated around the critical stretching factor due to latent heat effects and the strength of the lower crust changes upon embrittlement. The value of the critical stretching factor depends on the rift duration and ranges from $\sim$5 for a rift duration of 5 Ma to $\sim$3 for a rift duration of 30 Ma.

[26] These patterns change if sedimentation is included. Figure 6 (middle) shows the same simulations as before but with a constant sedimentation rate of 0.2 mm/yr. Sediment deposition results in higher Moho temperatures and lower crustal viscosities. As a consequence, complete crustal embrittlement occurs only for higher stretching factors. In fact, the shift of the critical stretching factor to higher values scales with the thickness of synrift sediments that are shown as black contours in Figures 6e and 6f. In addition, the higher Moho temperatures result in a reduced volume of sub-Moho mantle that is within the thermal stability field of serpentine (Figure 6f).

[27] The interrelation between sedimentation, the rheological evolution of the lower crust, and mantle serpentinization becomes even clearer, when

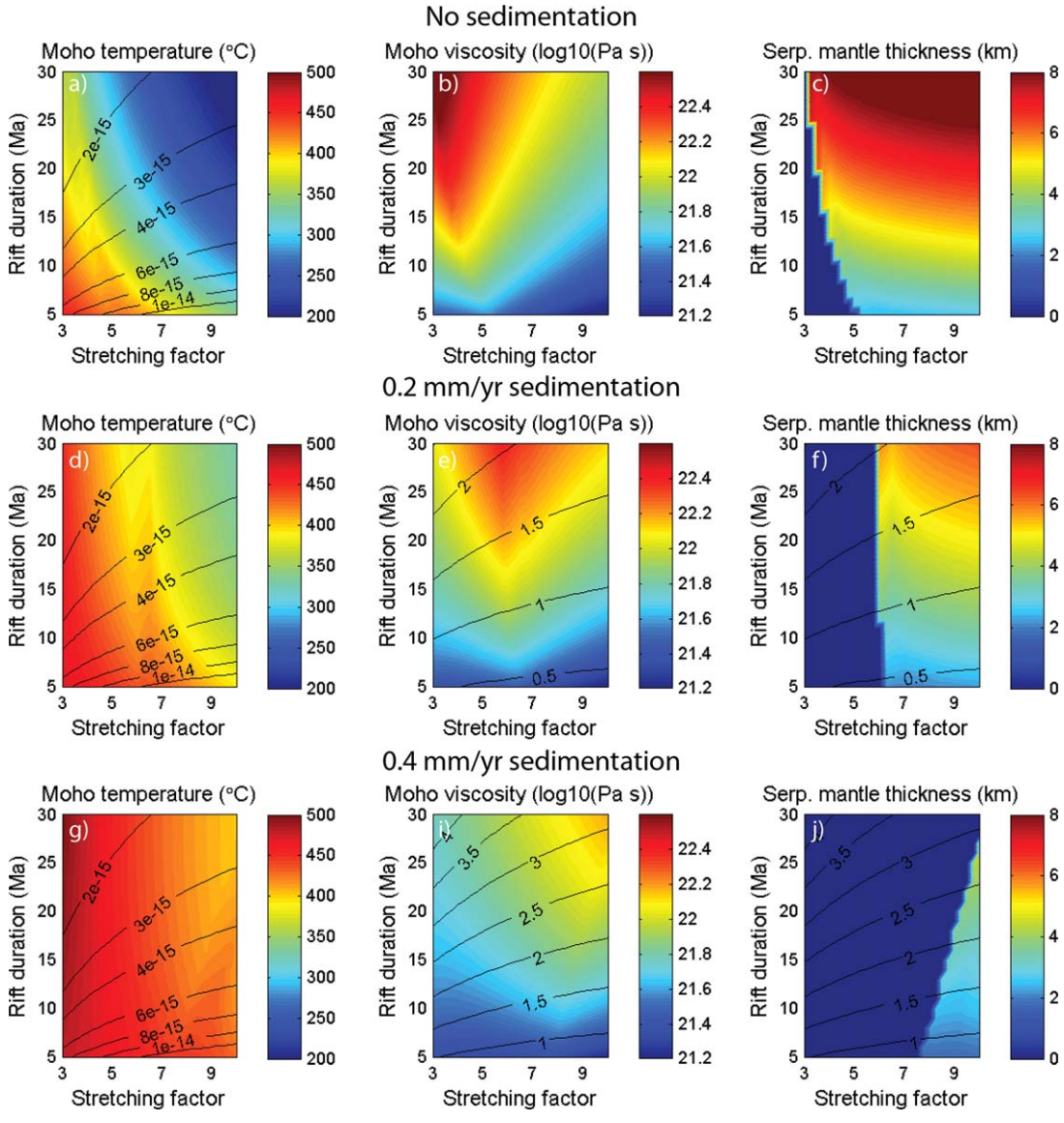

Figure 6. Effects of sediment supply on the rheological evolution of the lower crust and the onset and extent of mantle serpentinization. Each figure is based on 754 individual model runs. The black contours on the left plot show strain rates in s^{-1}. The black contours lines in the middle and right plot show sediment thickness in km.

the sedimentation rate is doubled to a value of 0.4 mm/yr. Figure 6 (bottom) illustrates this case: Moho temperatures are even higher and crustal embrittlement only occurs for extremely high stretching factors. These simulations clearly show the first order effects that sediments have on the rheological evolution of the lower crust and thereby on serpentinization. Figure 6 also illustrates another effect of sedimentation: the thicker the sedimentary cover, the higher is the sub-Moho mantle temperature. This blanketing effect, discussed in more detail in *Theissen and Rüpke* [2010], shows that the sub-Moho mantle is hotter beneath sedimented margins with respect to sediment-starved margins—a finding true for both the out-of-equilibrium synrift and equilibrium late postrift situation. This may have important implications for the strength of curst and mantle, strain partitioning during rifting, and possibly even mantle melting processes.

3.3. Discussion

[28] We have shown how stretching, faulting, sedimentation, and mantle serpentinization affect each other. The findings of the numerical experiments

without sedimentation basically confirm and reproduce the results of *Perez-Gussinye and Reston* [2001]. The simulations with sedimentation show the strong control of sediment supply on the strength of the lower crust. The higher the sedimentation rate (and thicker the sediment cover), the hotter and weaker is the crust, and the less likely are complete crustal embrittlement and consequently mantle serpentinization reactions. These findings are summarized in Figure 1, which shows the temporal evolution of three example model runs with a stretching factor of 8, a rift duration of 20 Ma, and different sedimentation rates (0, 0.2, and 0.4 mm/yr). These simulations are taken from the larger set of simulations that are shown in Figure 6. In the case without sediments (Figure 1a), the lower crust turns brittle upon a critical stretching factor of 3.9 thereby permitting mantle serpentinization. The sub-Moho mantle is relatively cold illustrated by the location of 550°C isotherm. If the sedimentation rate is increased to 0.2 mm/yr (Figure 1b), the situation changes and the lower crust turns brittle at a higher critical stretching factor of 5.9. The sub-Moho mantle is hotter due to blanketing effects. Finally, for a sedimentation rate of 0.4 mm/yr parts of the lower crust remain ductile throughout the entire simulation and mantle serpentinization is not possible (Figure 1c). The sub-Moho mantle is even hotter than in (Figure 1b). This shows that with increased sedimentation rates, the strength of the lower crust decreases and serpentinization reactions become less likely.

[29] The strong control of sediment supply on crustal strength has important consequences for the dynamics of passive margin formation. Observations and simulations of lithosphere dynamics during continental rifting point to the strength of the lower crust as a key factor controlling the geometry of passive margins [*Huismans and Beaumont*, 2011; *Ranero and Perez-Gussinye*, 2010]. A weak lower crust results in wide south-Atlantic type margins, while a relatively strong lower crust results in Iberia-Newfoundland type margins. Our simulations are consistent with these previous ideas and clearly show that the rate of sediment supply controls the strength of the lower crust, which may thus play a key role in switching between these end-members.

4. Implications for the Mid-Norwegian Margin

[30] The preceding sections describe feedbacks between shallow sedimentary and deep mantle processes. The relevance of these feedbacks for different margins around the world needs to be assessed in case studies and as a first step in this direction we have explored the likeliness of mantle serpentinization during the formation of the mid-Norwegian volcanic margin. As the above findings illustrate, mantle serpentinization is only likely when stretching factors are high and sediment supply is limited. We will test if such conditions may have occurred during the formation of the Norwegian volcanic margin and evaluate whether lower crustal bodies imaged beneath the margin may, in fact, be partially serpentinized mantle.

4.1. Geological Setting and Input Data

[31] The Møre and Vøring continental margin, situated between 61°N and 68°N and 2°E and 10°E, is commonly considered an end-member of a volcanic rifted margin, where late rifting and breakup were accompanied by strong intrusive and extrusive magmatic activity [*Ren et al*., 2003]. Major tectonic subunits include the Trøndelag platform with thick pre-Cretaceous sedimentary units, the deep Cretaceous Møre and Vøring basins, and the marginal highs close to the continent-ocean-transition (COT). The post-Caledonian evolution of the margin is characterized by extensional tectonics that cumulated in breakup and the opening of the North Atlantic in early Eocene times. The number and timing of rift episodes are still debated but there is an agreement on a major rift event during the late Jurassic [*Brekke*, 2000; *Doré et al*., 1999] and on the onset of seafloor spreading at about 55 Ma [*Faleide et al*., 2008]. A debate continues on a possible rift phase in the mid-Cretaceous. *Fjeldskaar et al*. [2008] described stratigraphic evidence in the Vøring Basin and modeled an extension event at 95 Ma, whereas *Skogseid et al*. [2000] and *Faerseth and Lien* [2002] argued that there is no evidence for mid-Cretaceous extension in the Vøring Basin. We assume here that no rifting occurred throughout the Cretaceous—an assumption that has implications for the amount and rate of rifting during the late Jurassic.

[32] The target area of this study is shown as a black box in Figure 7 and comprises large parts of the Møre and Vøring basins and extends into oceanic crust. For this area, *Scheck-Wenderoth and Maystrenko* [2011] compiled a continuous data set on the crustal configuration and thicknesses of various sedimentary sequences based on publically available seismic data. This data set describes six sedimentary units which they describe as: upper

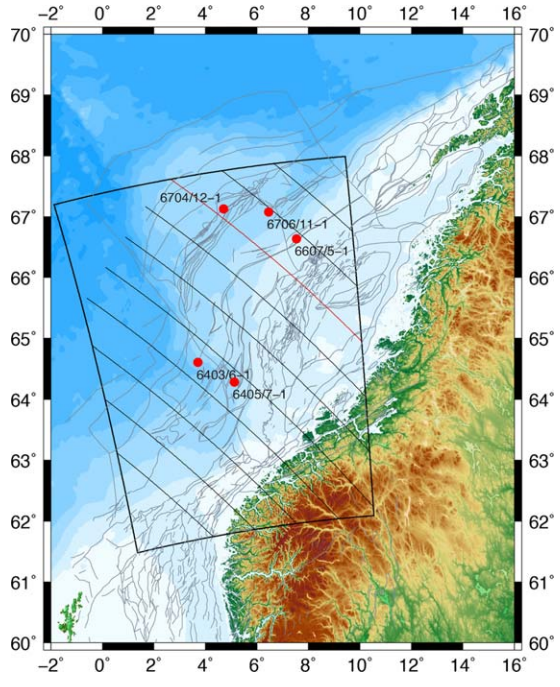

Figure 7. Base map of the study area. The black box shows the extent of the 3-D data set. The structural elements of the margin are taken from *Blystad et al*. [1995]. Ten transects are used to reconstruct the margin and five wells are used for thermal calibration. The transect marked in red is the one that is shown Figure 8. The plot was made with GMT in geographical coordinates using a cylindrical equidistant projection with 10° as central meridian on a WGS84 ellipsoid.

Neogene (postmiddle Miocene), middle-upper Paleogene-lower Neogene (premiddle Miocene), lower Paleogene (Paleocene), Upper Cretaceous (post-Cenomanian), Lower Cretaceous (pre-Cenomanian), pre-Cretaceous. These sedimentary units form the input for the TecMod reconstructions and have been assigned the following ages: 16, 56, 66, 93.5, 145.5, and 176 Ma. Note that 260 Ma and not 176 Ma is the commonly used age for the top basement and the onset of extension. However, we need stratigraphic information to model the duration and magnitude of individual rift events. Instead of assuming an unrealistically long rift event from 260 to 145.5 Ma, we used a younger age for the onset of rifting. This has almost no effect on the cumulative amount of stretching at the end of the Jurassic but ensures that no artificially low strain rates (and basin temperatures) are assumed, which would overestimate the likeliness of complete crustal embrittlement and therefore serpentinization.

[33] The data set by *Scheck-Wenderoth and Maystrenko* [2011] further includes the oceanic layers 2A, 2B, 3A, and 3B, which we simply combine into a single oceanic crust layer. Of special importance are "high density bodies within the lower crystalline crust" and "high-density zones within the continental crystalline crust" (in the terminology of *Scheck-Wenderoth and Maystrenko* [2011]). We will refer to the former ones as outer LCBs and to latter ones as inner LCBs.

[34] No single accepted hypothesis exists for the nature and origin of LCBs beneath the Møre and Vøring margin. The outer LCBs, close to the COT, are clearly visible in seismic refraction data as high-velocity bodies [e.g., *Mjelde et al*., 2001], and have consequently also been interpreted as high-density bodies. Those outer LCBs are often thought to be breakup-related underplates of mantle melts [*Fjeldskaar et al*., 2008; *Gernigon et al*., 2004; *Maystrenko and Scheck-Wenderoth*, 2009]. While a magmatic origin is consistent with the excess magmatism close to the COT and the continuity between the LCBs and oceanic layer 3B, also other hypotheses exist for some of the outer LCBs including serpentinized mantle and dismembered eclogites (see *Gernigon et al*. [2004], for a summary). While clear seismic evidence exist for the outer LCBs, the case for separate inner LCBs is not as clear. Hints from seismic data on distinct inner LCBs exist for the Møre margin [*Mjelde et al*., 2009] but most information on their location and extent stem from gravity modeling [*Maystrenko and Scheck-Wenderoth*, 2009; *Reynisson et al*., 2010]. Nevertheless, the inner LCBs, as defined in the data set by *Maystrenko and Scheck-Wenderoth* [2009], follow the Caledonian structural trend and are located in areas not affected by breakup related melting. The correlation between major faults affecting the base Cretaceous and thickness variations of these inner LCBs can also be seen in Figures 8 and 12. Different hypotheses exist also for the origin of the inner LCBs including partially serpentinized mantle [*Lundin and Dore*, 2011; *Reynisson et al*., 2010], heterogeneous continental crust [*Ebbing et al*., 2009], and eclogite bodies [*Mjelde et al*., 2012]. We use our new basin modeling framework to test the first hypothesis and explore whether mantle serpentinization can occur during margin formation. Despite the discussed uncertainties, the Møre and Vøring margin remains, in fact, a good candidate for our case study. The multistage rift history with severe crustal thinning and strong variations in sedimentation rates permit exploring feedbacks between shallow sedimentary and deep mantle processes. The internally consistent data set by *Scheck-*

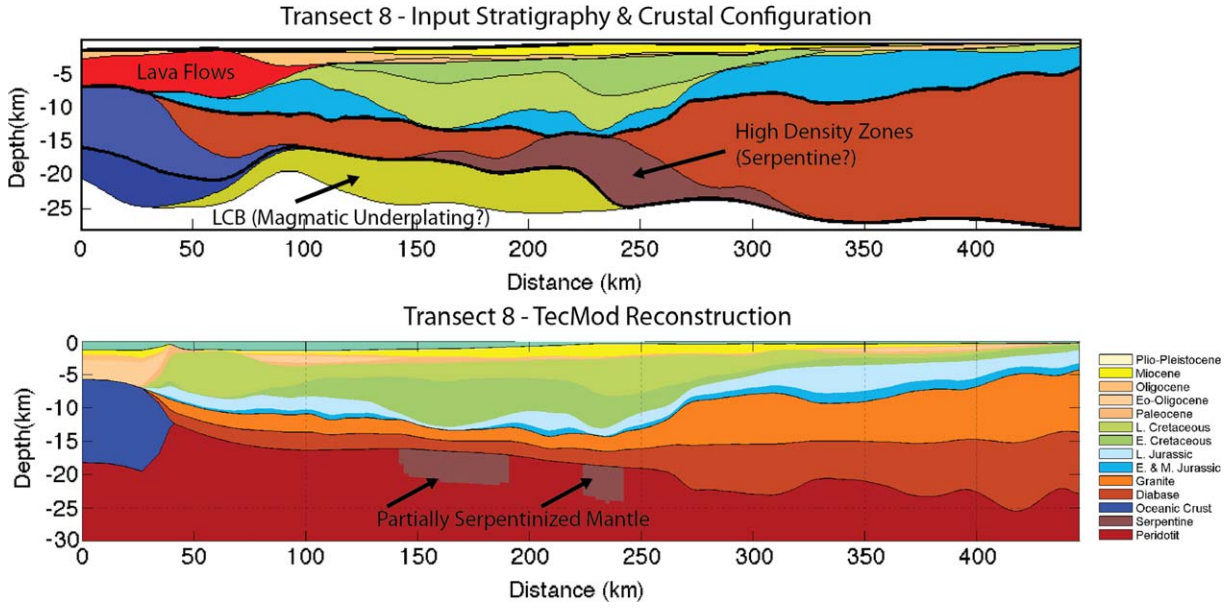

Figure 8. The top plot shows the input data for transect 8. The bottom plot shows the reconstructed transect and serpentine underplates. The location of the transect is shown as a red line in Figure 7.

Wenderoth and Maystrenko [2011] allows us to test whether predictions on mantle serpentinization from basin modeling are consistent with observations on the inner lower crustal bodies.

4.2. Model Setup

[35] We have extracted 10 transects across the Møre and Vøring basins (Figure 7) and used them as input for TecMod based thermotectonostratigraphic reconstructions. This multislice approach allows us to map out possible serpentine bodies beneath this part of the Norwegian margin. The setup of the 2-D reconstructions is largely the same as in the synthetic model runs discussed in section 3.2. The only differences are that the radiogenic heat production was reduced to 2.5×10^{-6} W/m^3 (to fit observed well temperatures and vitrinite reflectance values) and that flexural isostacy is assumed with an effective elastic thickness of 5 km and a necking level of 10 km (to better match the seismically observed crustal configuration). Breakup in all transects that extend into oceanic crust occurs at 55 Ma and 15 km thick oceanic crust is formed. Magmatic underplating and extrusive lava flows are not considered in the reconstructions. The rock properties used in the case study are described in Table 3.

4.3. Structural and Thermal Evolution of the Margin

[36] Figure 8 (top) shows, as an example, the input stratigraphy (and input crustal configuration) for

Table 3. Rock Properties for the Møre/Vøring Case Study

Lithology	Density (kg/m^3)	Thermal Exp. (1/K)	Rad. Heating (W/m^3)	Heat Capacity (J/kg/K)	Grain Cond. (W/m/K)	Porosity	Inv. Comp. Length (1/km)
Peridotite	3300	3.20E−05	0.00	1288	3.4	0	0
Oceanic crust	2700	2.40E−05	0.00	1000	2.5	0	0
Upper crust	2800	2.40E−05	2.50E−06	1116	2.5	0	0
Lower crust	2850	2.40E−05	2.50E−06	1116	2.5	0	0
E. and M. Jurassic	2720	0.00	1.00E−06	855	4.0	0.41	0.31
L. Jurassic	2500	0.00	1.00E−06	900	3.2	0.39	0.33
E. Cretaceous	2600	0.00	1.00E−06	900	2.1	0.59	0.44
L. Cretaceous	2700	0.00	1.00E−06	860	1.9	0.6	0.46
Paleocene	2650	0.00	1.00E−06	880	4	0.42	0.28
Eo-Oligocene	2720	0.00	1.00E−06	855	4	0.41	0.31
Oligocene	2700	0.00	1.00E−06	820	4	0.42	0.3
Miocene	2680	0.00	1.00E−06	870	4.6	0.41	0.28
Plio-Pleistocene	2720	0.00	1.00E−06	855	4	0.41	0.31

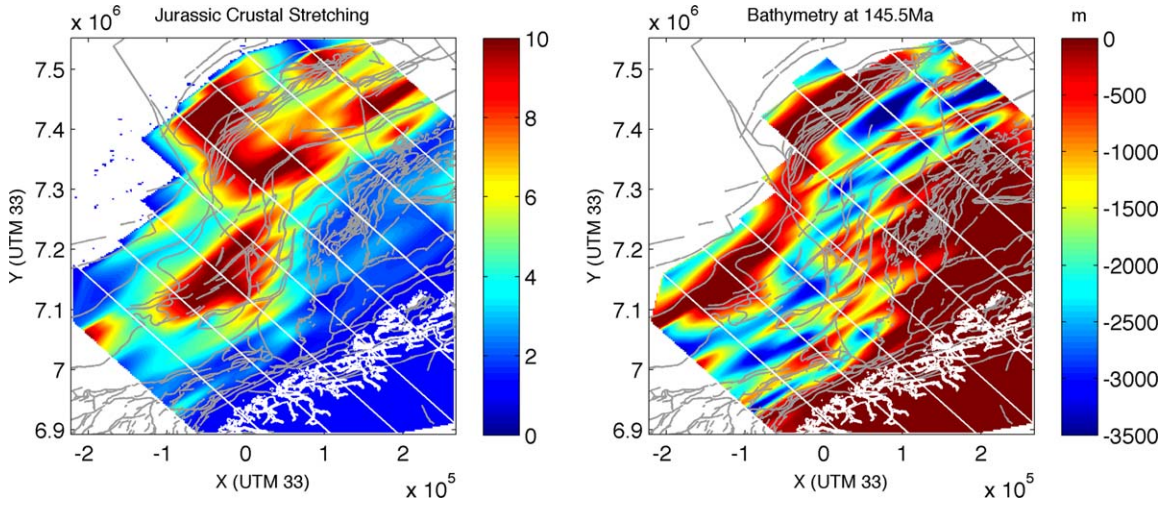

Figure 9. Jurassic stretching factors and paleobathymetry at Base Cretaceous time. All data are gridded from the 10 transects onto present-day coordinates. This white lines mark the modeled transects and thick white lines the Norwegian coastline. Maps are in UTM coordinates (zone 33W) on a WGS84 ellipsoid.

the transect marked as red in Figure 7 across the Vøring basin. Figure 8 (bottom) shows the reconstructed transect. Both the stratigraphy and the overall crustal configuration are fitted well. All other nine transects show equally good fits to the input data. Figure 9 shows a map of predicted cumulative crustal stretching factors at the end of the Jurassic rift phase, which reach values of up to 10 beneath the deepest basins. The high Jurassic stretching factors are, in part, a consequence of our two-rift phase scenario that does not include Cretaceous rifting. All the accommodation space for the thick Cretaceous sediment sequences must be created during the Jurassic rift phase. This results in deep water conditions at base Cretaceous time (Figure 9). Note that the reconstructions already account for reaction-induced uplift in areas affected by mantle serpentinization processes. A model without serpentinization would result in slightly less stretching in order to create the same accommodation space. A hypothetical significant Late Cretaceous rift phase would result in somewhat lower Jurassic stretching factors and shallower Base Cretaceous water depth values.

[37] The good fits between input and reconstructed stratigraphies are quality checks of the structural solution. The thermal solution can be independently benchmarked through well calibration. For five wells (Figure 7), we have compiled publically available temperature and vitrinite reflectance data. Figure 10 shows that the obtained thermal solution is consistent with both well temperature data as well as vitrinite reflectance values. This establishes confidence in the thermal solution and suggests that the thermal parameters (e.g., thermal conductivity, radiogenic heat production) as well as the predicted basement heat flow evolution are consistent with observations. The thermal and tectonic solutions thus appear valid approximations for the formation and evolution of the Norwegian margin that can be interpreted in terms of possible mantle serpentinization processes.

4.4. Serpentinization During Margin Formation

[38] The systematic study on the interrelation between rifting, sedimentation, and serpentinization has shown that crustal embrittlement and therefore mantle serpentinization can only occur if sediment thicknesses are low and stretching factors are high. With regard to the Norwegian margin the most favorable conditions for serpentinization exist at the end of the dominant Jurassic rift phase beneath the deep Cretaceous basins with little pre-Cretaceous sediments. Figure 11 exemplifies the conditions at Base Cretaceous time. The top plot shows deep-water conditions with little sedimentary cover beneath the future Cretaceous basins. Sub-Moho mantle temperatures are well below the thermal stability limit within the central rift zone. These are favorable conditions for serpentinization and the middle plot in Figure 11 confirms this by showing that the entire crust has become brittle. The bottom plot shows that two distinct serpentine bodies form beneath the main rift zones. The density of these partially serpentinized (~20%) mantle bodies is ~3200 kg/m^3, which is roughly consistent with the density of the

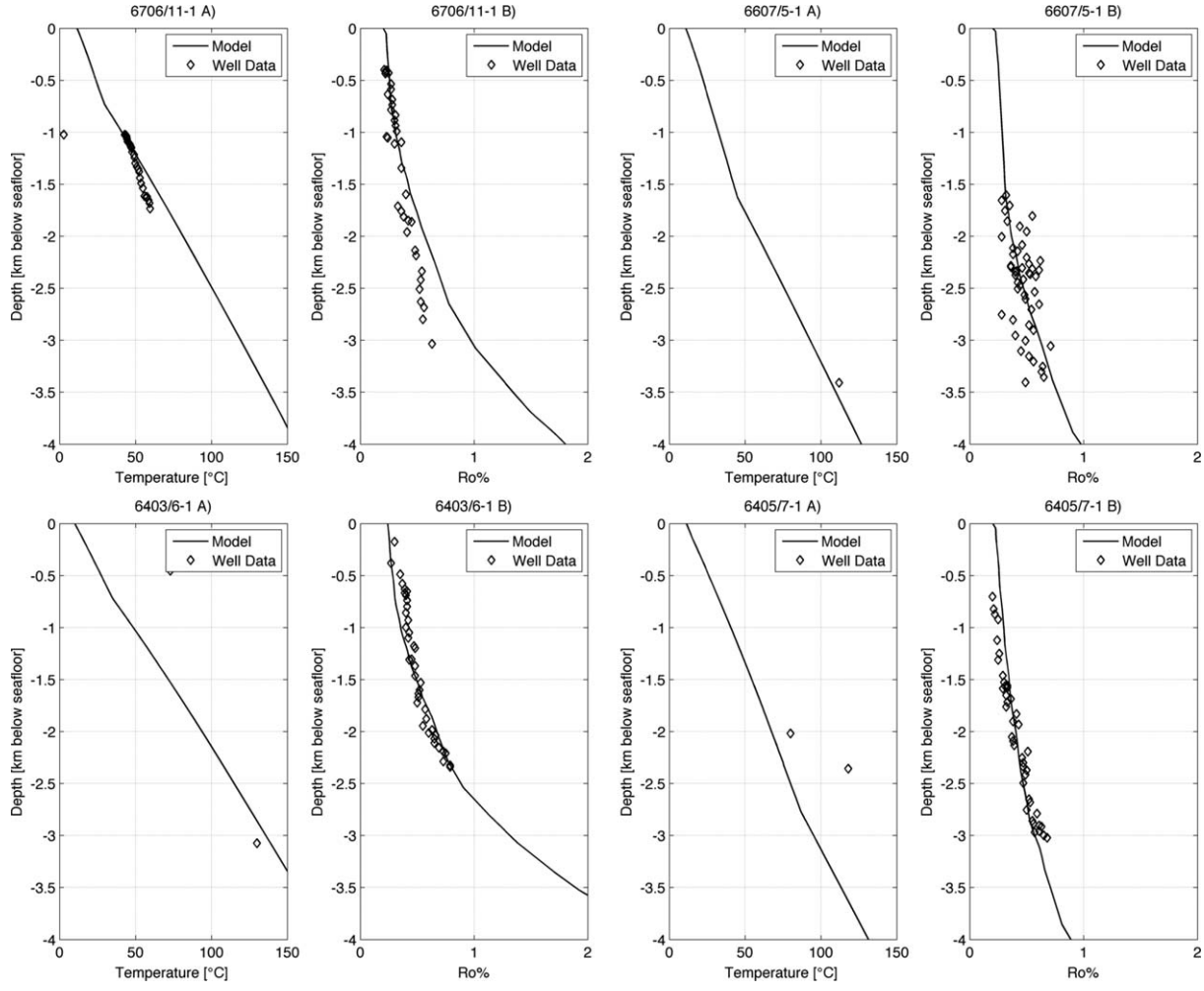

Figure 10. Well calibration. All left plots show computed present-day temperatures as black lines and measured well temperatures as symbols. All right plots show computed vitrinite reflectance values (EASY%Ro) as black lines and well data as symbols. The vertical scale refers to kilometers below the seafloor.

inner LCBs inferred from gravity data [*Maystrenko and Scheck-Wenderoth*, 2009]. It thus seems that serpentinization reaction may, in fact, take place at the end of the Jurassic rift phase.

[39] In order to further test this idea, we have gridded the predicted serpentine bodies from all 10 transects onto UTM coordinates. Figure 12 shows a comparison between the locations and thicknesses of the inner LCBs in the input data and the predicted serpentine underplates. Although the fit is not perfect, a clear spatial and thickness correlation between the two maps exists. The predicted serpentine underplates follow, just like the inner LCBs, a general North-East to South-West trend along the major Jurassic faults. There is a slight seaward offset in the location of the predicted serpentine bodies with respect to the observed inner LCBs. This offset may results from low-angle detachment faulting known to occur in this area, whose kinematics may not be completely captured by our pure-shear model.

4.5. Discussion

[40] The reconstruction of multiple transects across the Møre and Vøring basin has shown that complete crustal embrittlement is likely to occur during the Jurassic rift phase. Such crust-cutting faults are in fact observed in seismic data [*Osmundsen and Ebbing*, 2008; *Osmundsen et al*., 2002] making it a plausible prediction. Furthermore, the existence of inner and outer LCBs has also been inferred by a number of seismic and gravity studies [*Maystrenko and Scheck-Wenderoth*, 2009; *Mjelde et al*., 2005; *Raum et al*., 2006; *Reynisson et al*., 2010]. The question is how likely a serpentinized mantle origin is for those inner LCBs. Close to the continent

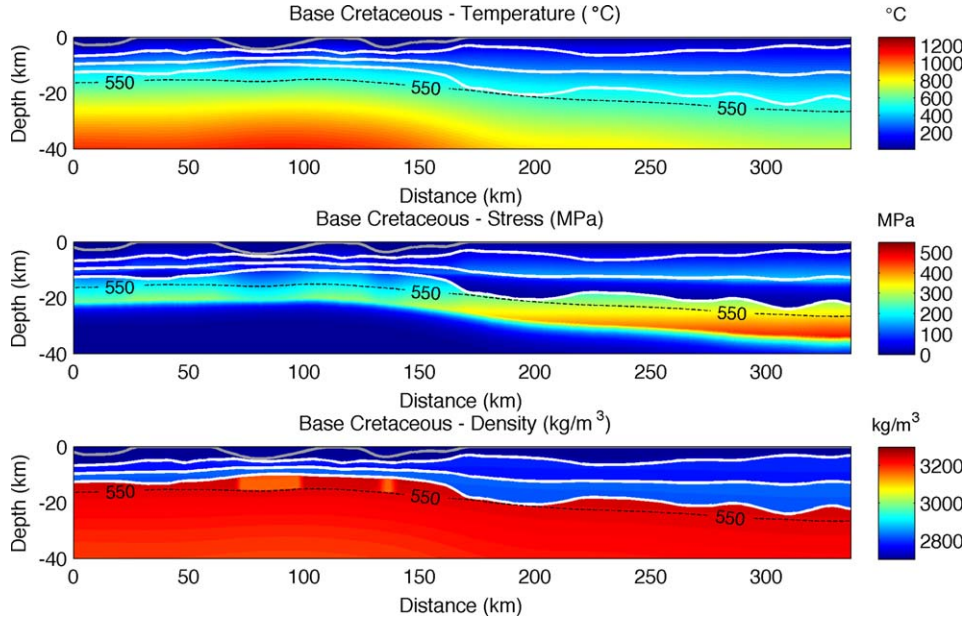

Figure 11. During the Jurassic rift phase parts of the extending continental crust become entirely brittle so that mantle serpentinization can occur. (top) temperature, (middle) differential stress, and (bottom) density. White lines mark the crustal geometry and the top grey line marks the seafloor.

ocean transition temperatures were likely too high at the time of breakup for serpentine to form or to remain stable. In addition, the continuity between of the outer LCBs and the oceanic layer 3B suggests a breakup related mantle melting origin [*Maystrenko and Scheck-Wenderoth*, 2009]. The situation is different for the inner LCBs. Previous studies already pointed to a possible serpentinized mantle origin [*Lundin and Dore*, 2011; *Osmundsen and Ebbing*, 2008; *Reynisson et al*., 2010]. Here we now present support for this hypothesis from integrated basin modeling. Our results show that complete crustal embrittlement may in fact take place during the Jurassic rift phase, which is the key prerequisite for serpentinization to occur. However, only the close integration of models and data will be able to test this idea more rigorously. For example, depending on the amount of magnetite

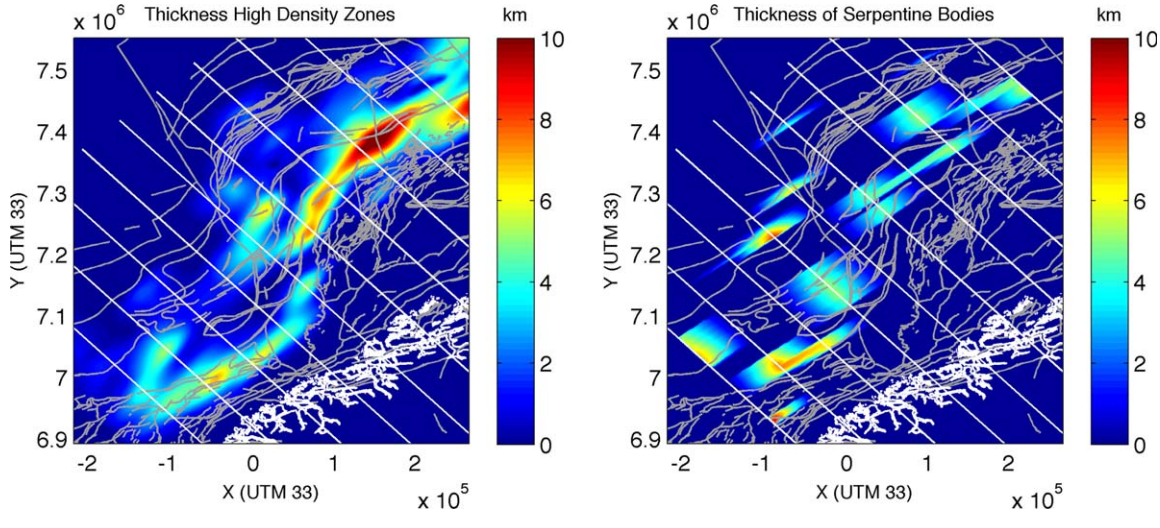

Figure 12. (left) The thickness of "high density zones", which are inferred from seismic and gravity data [*Maystrenko and Scheck-Wenderoth*, 2009]. Note that the thickness and location of the outer LCBs is not shown. (right) The predicted distribution and thickness of partially serpentinized mantle. Thin white lines mark the modeled transects and thick white lines the Norwegian coastline. Plots were made with Matlab in UTM coordinates (zone 33W) on a WGS84 ellipsoid.

forming during the reaction, partially serpentinized rocks have low densities and high magnetic susceptibilities. *Ebbing et al*. [2009] used a joint thermal modeling and potential field approach for the mid-Norwegian margin and found that the depth of the magnetized layer mainly correlates with the overall basement geometry and not the depth of the Curie temperature. While this may appear somewhat contradictory to our findings, our predicted degrees of partial serpentinization will not make a strong magnetic signal [*Malvoisin et al*., 2012a; *Oufi et al*., 2002]. In addition, given the complex geology of the mid-Norwegian margin it appears unlikely that all LCBs imaged beneath the margin share the same formation process. Our results show that serpentinization reactions are physically possible but they cannot provide a final answer on whether mantle serpentinization really occurs. It will be the future tighter integration of basin models like the one presented here with joint gravity/magnetics studies designed to explore for serpentine bodies at depth [*Fichler et al*., 2011; *Reynisson et al*., 2010] that provide additional insights and help to further evaluate the likeliness of mantle serpentinization during the formation of the Norwegian margin.

[41] Crustal scale faulting and associated mantle serpentinization reactions are typically associated with Iberian-type rifted margins [*Perez-Gussinye and Reston*, 2001; *Peron-Pinvidic and Manatschal*, 2009]. It now seems that similar processes may have been active during the Jurassic rift phase of the Norwegian margin. While the fundamentally different structures between volcanic and nonvolcanic margins continue to highlight their different natures and origins, our findings suggest that the mechanics of volcanic margin formation should, in part, be reviewed. First, the case study for the Norwegian margin has shown that a margin that is categorized as a volcanic margin due to the volcanic Paleocene/Eocene rift phase that resulted in breakup may, in fact, have experienced a nonvolcanic rift (margin) phase during the Jurassic with hyperextension of the crust and partial mantle serpentinization. As serpentine is a very weak mineral [*Hilairet et al*., 2007], the formation of partially serpentinized bodies will have a strong effect on strain partitioning. In fact, *Lundin and Dore* [2011] suggested that those parts of the Norwegian margin underlain by partially serpentinized mantle may be more prone to (compressional) deformation. Second, our findings highlight the importance of accurately resolving the thermal effects of sedimentation. The thickness of sediments and the rate of their deposition control the thermal structure of the entire extending lithosphere through blanketing effects: the thicker the sediment package and the lower its effective thermal conductivity, the higher are the average crustal and mantle temperatures (see also *Theissen and Rüpke* [2010]). The consequence is that sedimentation, through the temperature dependence of the viscous flow laws, has strong effects on the strength of the crust and in particular the lower crust, which in turn is likely to control the geometry of continental margins [*Huismans and Beaumont*, 2011; *Ranero and Perez-Gussinye*, 2010]. With respect to the Norwegian margin this implies that the strength and thermal structure of the lithosphere has been significantly different prior to the Jurassic rift and the successful Paleocene/Eocene rift phase that resulted in continental breakup. On the one hand, the Jurassic rift phase stretched a lithosphere with relatively thick crust, few sediments, and cold mantle, while the Paleocene/Eocene phase, in part, affected a prethinned lithosphere with thicker sediment packages and a hotter mantle. On the other hand, this effect is probably mitigated by the progressive seaward migration of the rift axis toward "less-stretched" lithosphere. While these considerations may hint at a more fundamental role of sediment supply in facilitating continental breakup, it will be up to future dynamic models to fully explore the feedbacks between sedimentation, strain partitioning, mantle serpentinization, and mantle melting.

[42] Finally, the alternative interpretation of LCBs as serpentinized mantle instead of magmatic underplates implies a fundamentally different thermal evolution of the Norwegian margin. The "emplacement" temperature of serpentine is $<550°C$, while magmatic LCBs intrude at temperatures $>1100°C$. Our alternative interpretation of the inner LCBs therefore opens the possibility of a colder margin evolution than previously thought. Furthermore, the timing of the LCB formation is completely different between the two alternatives—the transition between the Jurassic and the Cretaceous in the case of serpentinization versus the Paleocene for magmatic underplates.

5. Conclusions

[43] We have implemented serpentinization reactions into a two-dimensional thermotectono stratigraphic basin model. This allows us to quantitatively explore the causes and consequences of mantle serpentinization reactions during the formation of passive continental margins. The key findings of our study are:

[44] Mantle serpentinization occurs at stretching factors beyond a critical value upon which the

entire extending crust becomes brittle. Sedimentation leads to higher Moho temperatures and reduced lower crustal viscosities so that the critical stretching factor is shifted to higher values. This implies that the rate of sediment supply has first order control on the rheological evolution of the lower crust.

[45] The petrophysical changes associated with the partial serpentinization of mantle rocks have important thermal and isostatic consequences. Late synrift uplift may occur due to the density reduction and the release of latent heat enhances the synrift heat flow. These effects should be considered in the interpretation of subsidence and heat flow data above lower crustal bodies.

[46] This comprehensive multi-2-D reconstruction of the Norwegian Møre and Vøring margin shows that the margin may have undergone a nonvolcanic rift phase during the Jurassic with severe crustal thinning leading to complete crustal embrittlement and mantle serpentinization. The predicted locations and thicknesses of partially serpentinized mantle bodies correlate with LCBs inferred from gravity and seismic data. It thus seems that some of the inner LCBs along the Norwegian margin may well be partially serpentinized mantle, which would require a reassessment of both the timing as well as the thermal and isostatic consequences of LCB emplacement.

Acknowledgments

[47] We thank Magdalena Scheck-Wenderoth, an anonymous reviewer, and the editor Thorsten Becker for a very constructive, helpful, and speedy review process.

References

Blystad, P., H. Brekke, R. B. Færseth, B. T. Larsen, J. Skogseid, and B. Tørudbakken (1995), Structural elements of the Norwegian continental shelf. Part II: The Norwegian Sea Region, *Norwegian Petrol. Directorate Bull.*, *8*, 45.

Boillot, G., and N. Froitzhelm (2001), *Non-volcanic Rifted Margins, Continental Break-up and the Onset of Sea-floor Soreading: Some Outstanding Questions*, Geol. Soc. Lond.

Brekke, H. (2000), The tectonic evolution of the Norwegian Sea continental margin with emphasis on the Vøring and Møre Basins, in *Dynamics of the Norwegian Margin, vol. 167*, edited by A. Nøttvedt, pp. 327–378, Geol. Soc. Spec. Publ., The Geological Society London.

Deming, D., and D. S. Chapman (1989), Thermal histories and hydrocarbon generation—Example from Utah-Wyoming thrust belt, *AAPG Bull.*, *73*(12), 1455–1471.

Doré, A. G., E. R. Lundin, L. N. Jensen, ø. Birkeland, P. E. Eliassen, and C. Fichler (1999), Principal tectonic events in the evolution of the northwest European Atlantic margin, in *Petroleum Geology of Northwest Europe: Proceedings of the 5th Conference*, vol. *1*, edited by A. J. Fleet and S. A. R. Boldy, pp. 41–62, Geol. Soc. Lond.

Ebbing, J., L. Gernigon, C. Pascal, O. Olesen, and P. T. Osmundsen (2009), A discussion of structural and thermal control of magnetic anomalies on the mid-Norwegian margin, *Geophys. Prospect.*, *57*(4), 665–681.

Emmanuel, S., and B. Berkowitz (2006), Suppression and stimulation of seafloor hydrothermal convection by exothermic mineral hydration, *Earth Planet. Sci. Lett.*, *243*(3–4), 657–668.

Faerseth, R. B., and T. Lien (2002), Cretaceous evolution in the Norwegian Sea—A period characterized by tectonic quiescence, *Mar. Pet. Geol.*, *19*(8), 1005–1027.

Faleide, J. I., F. Tsikalas, A. J. Breivik, R. Mjelde, O. Ritzmann, O. Engen, J. Wilson, and O. Eldholm (2008), Structure and evolution of the continental margin off Norway and Barents Sea, *Episodes*, *31*(1), 82–91.

Fichler, C., T. Odinsen, H. Rueslatten, O. Olesen, J. E. Vindstad, and S. Wienecke (2011), Crustal inhomogeneities in the Northern North Sea from potential field modeling: Inherited structure and serpentinites?, *Tectonophysics*, *510*(1–2), 172–185.

Fjeldskaar, W., H. M. Helset, H. Johansen, I. Grunnaleiten, and I. Horstad (2008), Thermal modelling of magmatic intrusions in the Gjallar Ridge, Norwegian Sea: Implications for vitrinite reflectance and hydrocarbon maturation, *Basin Res.*, *20*(1), 143–159.

Fruh-Green, G. L., D. S. Kelley, S. M. Bernasconi, J. A. Karson, K. A. Ludwig, D. A. Butterfield, C. Boschi, and G. Proskurowski (2003), 30,000 years of hydrothermal activity at the Lost City vent field, *Science*, *301*(5632), 495–498.

Geoffroy, L. (2005), Volcanic passive margins, *C. R. Geosci.*, *337*(16), 1395–1408.

Gernigon, L., J. C. Ringenbach, S. Planke, and B. Le Gall (2004), Deep structures and breakup along volcanic rifted margins: Insights from integrated studies along the outer Voring Basin (Norway), *Mar. Pet. Geol.*, *21*(3), 363–372.

Gernigon, L., F. Lucazeau, F. Brigaud, J. C. Ringenbach, S. Planke, and B. Le Gall (2006), A moderate melting model for the Voring margin (Norway) based on structural observations and a thermo-kinematical modelling: Implication for the meaning of the lower crustal bodies, *Tectonophysics*, *412*(3–4), 255–278.

Hilairet, N., B. Reynard, Y. B. Wang, I. Daniel, S. Merkel, N. Nishiyama, and S. Petitgirard (2007), High-pressure creep of serpentine, interseismic deformation, and initiation of subduction, *Science*, *318*(5858), 1910–1913.

Huismans, R., and C. Beaumont (2011), Depth-dependent extension, two-stage breakup and cratonic underplating at rifted margins, *Nature*, *473*(7345), 74–78.

Iyer, K., L. H. Rüpke, and J. P. Morgan (2010), Feedbacks between mantle hydration and hydrothermal convection at ocean spreading centers, *Earth Planet. Sci. Lett.*, *296*(1–2), 34–44.

Koch, P. S. (1983), *Rheology and Microstructures of Experimentally Deformed Quartz Aggregates*, 464 pp., Univ. of Calif., Los Angeles.

Kronenberg, A. K., and J. Tullis (1984), Glow strengths of quartz aggregates—Grain-size and pressure effects due to hydrolytic weakening, *J. Geophys. Res.*, *89*(NB6), 4281–4297.

Lundin, E. R., and A. G. Dore (2011), Hyperextension, serpentinization, and weakening: A new paradigm for rifted margin compressional deformation, *Geology*, *39*(4), 347–350.

Malvoisin, B., J. Carlut, and F. Brunet (2012a), Serpentinization of oceanic peridotites: 1. A high-sensitivity method to monitor magnetite production in hydrothermal experiments, *J. Geophys. Res.*, *117*, B01104, doi:10.1029/2011JB008612.

Malvoisin, B., F. Brunet, J. Carlut, S. Rouméjon, and M. Cannat (2012b), Serpentinization of oceanic peridotites: 2. Kinetics and processes of San Carlos olivine hydrothermal alteration, *J. Geophys. Res.*, *117*, B04102, doi:10.1029/2011JB008842.

Martin, B., and W. S. Fyfe (1970), Some experimental and theoretical observations on the kinetics of hydration reactions with particular reference to serpentinization, *Chem. Geol.*, *6*, 185–202.

Maystrenko, Y., and M. Scheck-Wenderoth (2009), Density contrasts in the upper mantle and lower crust across the continent-ocean transition: Constraints from 3-D gravity modelling at the Norwegian margin, *Geophys. J. Int.*, *179*(1), 536–548.

Mjelde, R., P. Digranes, M. Van Schaack, H. Shimamura, H. Shiobara, S. Kodaira, O. Naess, N. Sørenes, and E. Vågnes (2001), Crustal structure of the outer Vøring Plateau, offshore Norway, from ocean bottom seismic and gravity data, *J. Geophys. Res.*, *106*(B4), 6769–6791.

Mjelde, R., T. Raum, B. Myhren, H. Shimamura, Y. Murai, T. Takanami, R. Karpuz, and U. Naess (2005), Continent-ocean transition on the Voring Plateau, NE Atlantic, derived from densely sampled ocean bottom seismometer data, *J. Geophys. Res.*, *110*, B05101, doi:10.1029/2004JB003026.

Mjelde, R., T. Raum, A. Kandilarov, Y. Murai, and T. Takanami (2009), Crustal structure and evolution of the outer Møre Margin, NE Atlantic, *Tectonophysics*, *468*(1–4), 224–243.

Mjelde, R., A. Goncharov, and R. D. Müller (2012), The Moho: Boundary above upper mantle peridotites or lower crustal eclogites? A global review and new interpretations for passive margins, *Tectonophysics*, in press, doi: http://dx.doi.org/10.1016/j.tecto.2012.03.001.

Newman, R., and N. White (1997), Rheology of the continental lithosphere inferred from sedimentary basins, *Nature*, *385*(6617), 621–624.

Osmundsen, P. T., and J. Ebbing (2008), Styles of extension offshore mid-Norway and implications for mechanisms of crustal thinning at passive margins, *Tectonics*, *27*(6), doi:10.1029/2007TC002242.

Osmundsen, P. T., A. Sommaruga, J. R. Skilbrei, and O. Olesen (2002), Deep structure of the Mid Norway rifted margin, *Norwegian J. Geol.*, *82*(4), 205–224.

Oufi, O., M. Cannat, and H. Horen (2002), Magnetic properties of variably serpentinized abyssal peridotites, *J. Geophys. Res.*, *107*(B5), 2095, doi:10.1029/2001JB000549.

Perez-Gussinye, M., and T. J. Reston (2001), Rheological evolution during extension at nonvolcanic rifted margins: Onset of serpentinization and development of detachments leading to continental breakup, *J. Geophys. Res.*, *106*(B3), 3961–3975.

Perez-Gussinye, M., J. Morgan, T. Reston, and C. Ranero (2006), The rift to drift transition at non-volcanic margins: Insights from numerical modelling, *Earth Planet. Sci. Lett.*, *244*(1–2), 458–473.

Peron-Pinvidic, G., and G. Manatschal (2009), The final rifting evolution at deep magma-poor passive margins from Iberia-Newfoundland: A new point of view, *Int. J. Earth Sci.*, *98*(7), 1581–1597.

Ranalli, G., and D. C. Murphy (1987), Rheological stratification of the lithosphere, *Tectonophysics*, *132*(4), 281–295.

Ranero, C. R., and M. Perez-Gussinye (2010), Sequential faulting explains the asymmetry and extension discrepancy of conjugate margins, *Nature*, *468*(7321), 294–299.

Raum, T., R. Mjelde, H. Shimamura, Y. Mural, E. Brastein, R. M. Karpuz, K. Kravlk, and H. J. Kolsto (2006), Crustal structure and evolution of the southern Voring basin and voring transform margin, NE Atlantic, *Tectonophysics*, *415*(1–4), 167–202.

Ren, S. C., J. I. Faleide, O. Eldholm, J. Skogseid, and F. Gradstein (2003), Late Cretaceous-Paleocene tectonic development of the NW Voring Basin, *Mar. Pet. Geol.*, *20*(2), 177–206.

Reston, T. J., and K. G. McDermott (2011), Successive detachment faults and mantle unroofing at magma-poor rifted margins, *Geology*, *39*(11), 1071–1074.

Reynisson, R. F., J. Ebbing, E. Lundin, and P. T. Osmundsen (2010), Properties and distribution of lower crustal bodies on the mid-Norwegian margin, *Pet. Geol. Conf. Ser.*, *7*, 843–854.

Rüpke, L. H., S. M. Schmalholz, D. W. Schmid, and Y. Y. Podiadchikov (2008), Automated thermotectonostratigraphic basin reconstruction: Viking Graben case study, *AAPG Bull.*, *92*(3), 309–326.

Rüpke, L. H., D. W. Schmid, E. H. Hartz, and B. Martinsen (2010), Basin modelling of a transform margin setting: Structural, thermal and hydrocarbon evolution of the Tano Basin Ghana, *Pet. Geosci.*, *16*(3), 283–298.

Sawyer, D., M. Coffin, T. Reston, J. Stock, and J. Hopper (2007), COBBOOM: The Continental Breakup and Birth of Oceans Mission, *Sci. Drill.*, *5*, 13–25.

Scheck-Wenderoth, M., and Y. Maystrenko (2011), *3D lithospheric-scale structural model of the Norwegian continental margin (the Vøring and Møre basins) Rep*. STR11/02, GFZ Helmholtz Cent., Potsdam, Germany, doi:10.2312/GFZ.b103–11027.

Shelton, G., and J. Tullis (1981), Experimental flow laws for crustal rocks, *EoS Trans. AGU*, *62*(17), Fall Meet. Suppl.

Skelton, A., R. Whitmarsh, F. Arghe, P. Crill, and H. Koyi (2005), Constraining the rate and extent of mantle serpentinization from seismic and petrological data: Implications for chemosynthesis and tectonic processes, *Geofluids*, *5*(3), 153–164.

Skogseid, J., S. Planke, J. I. Faleide, T. Pedersen, O. Eldholm, and F. Neverdal (2000), NE Atlantic continental rifting and volcanic margin formation, *Dyn. Norwegian Margin*, *167*, 295–326.

Theissen, S., and L. H. Rüpke (2010), Feedbacks of sedimentation on crustal heat flow: New insights from the Vøring Basin, Norwegian Sea, *Basin Res.*, *22*(6), 976–990.

Tullis, T. E., F. G. Horowitz, and J. Tullis (1991), Flow laws of polyphase aggregates from end-member flow laws, *J. Geophys. Res.*, *96*(B5), 8081–8096.

Ulmer, P., and V. Trommsdorff (1995), Serpentine stability to mantle depths and subduction-related magmatism, *Science*, *268*(5212), 858–861.

Wegner, W. W., and W. G. Ernst (1983), Experimentally determined hydration and dehydration reaction rates in the system MgO-SiO_2-H_2O, *Am. J. Sci.*, *283-A*, 151–180.

White, R. S., G. D. Spence, S. R. Fowler, D. P. McKenzie, G. K. Westbrook, and A. N. Bowen (1987), Magmatism at rifted continental margins, *Nature*, *330*(6147), 439–444.

Whitmarsh, R. B., G. Manatschal, and T. A. Minshull (2001), Evolution of magma-poor continental margins from rifting to seafloor spreading, *Nature*, *413*(6852), 150–154.